

Effects of mesoscale eddies on the spatial coherence of a middle range sound field in deep water

Fei Gao(高飞), Fang-Hua Xu(徐芳华), and Zheng-Lin Li(李整林)

Citation: Chin. Phys. B, 2022, 31 (**11**): 114302. DOI: 10.1088/1674-1056/ac6014

What follows is a list of articles you may be interested in

Parallel optimization of underwater acoustic models: A survey

Zi-jie Zhu(祝子杰), Shu-qing Ma(马树青), Xiao-Qian Zhu(朱小谦), Qiang Lan(蓝强), Sheng-Chun Piao(朴胜春), and Yu-Sheng Cheng(程玉胜)

Chin. Phys. B, 2022, 31 (**10**): 104301. DOI: 10.1088/1674-1056/ac7ccc

Improving sound diffusion in a reverberation tank using a randomly fluctuating surface

Qi Li(李琪), Dingding Xie(谢丁丁), Rui Tang(唐锐), Dajing Shang(尚大晶), and Zhichao Lv(吕志超)

Chin. Phys. B, 2022, 31 (**6**): 064302. DOI: 10.1088/1674-1056/ac3812

Underwater acoustic metamaterial based on double Dirac cone characteristics in rectangular phononic crystals

Dong-Liang Pei(裴东亮), Tao Yang(杨洮), Meng Chen(陈猛), Heng Jiang(姜恒)

Chin. Phys. B, 2019, 28 (**12**): 124301. DOI: 10.1088/1674-1056/ab55d2

A novel multi-cavity Helmholtz muffler

Han-Bo Shao(邵瀚波), Huan He(何欢), Yan Chen(陈岩), Guo-Ping Chen(陈国平)

Chin. Phys. B, 2019, 28 (**5**): 054303. DOI: 10.1088/1674-1056/28/5/054303

Influence of warm eddies on sound propagation in the Gulf of Mexico

Yao Xiao(肖瑶), Zhenglin Li(李整林), Jun Li(李鋆), Jiaqi Liu(刘佳琪), Karim G Sabra

Chin. Phys. B, 2019, 28 (**5**): 054301. DOI: 10.1088/1674-1056/28/5/054301

Effects of mesoscale eddies on the spatial coherence of a middle range sound field in deep water

Fei Gao(高飞)[1,2,†], Fang-Hua Xu(徐芳华)[1], and Zheng-Lin Li(李整林)[3]

[1] *Department of Earth System Science, Ministry of Education Key Laboratory of Earth System Modeling, Institute for Global Change Studies, Tsinghua University, Beijing* 100084, *China*
[2] *Naval Research Institute, Tianjin* 300061, *China*
[3] *School of Ocean Engineering and Technology, Sun Yat-Sen University, Zhuhai* 519000, *China*

(Received 11 December 2021; revised manuscript received 21 March 2022; accepted manuscript online 23 March 2022)

Mesoscale eddies have a remarkable influence on the underwater sound field. Many previous studies have investigated the effects of eddies on transmission loss, the convergence zone, time delay, etc. However, the effects of eddies on spatial coherence are less well studied and remain unclear. In this paper, the effects of eddies on spatial coherence at the subsurface in deep water are investigated. The eddy environments are simulated with Gaussian eddy equations, the complex pressure field is obtained using a range-dependent parabolic equation model and the associated mechanism is analyzed based on ray theory and models. The results show that cold/warm mesoscale eddies affect spatial coherence in a high-intensity zone by changing the locations and width of the convergence zone. In the shadow zone, the horizontal correlation radius and the vertical correlation radius increase with range and decrease with depth, and they are increased by warm eddies and decreased by cold eddies, mainly caused by variation of the multipath structure.

Keywords: mesoscale eddy, horizontal coherence, vertical coherence, multipath arrivals

PACS: 43.30.+m, 43.30.Bp, 43.30.Cq, 92.10.Vz **DOI:** 10.1088/1674-1056/ac6014

1. Introduction

Spatial coherence, in a horizontal or vertical direction,[1,2] describes the level of similarity of an acoustic signal between two positions, and is usually quantified using a correlation coefficient.[3] With strong spatial coherence, the target signal with a small signal to noise ratio (SNR) can be recognized well, and this is crucial for SONAR signal processing, detection, localization and communication, etc. It is of great importance to understand the spatial coherence of sound fields.

Mesoscale eddies, ubiquitous in the world's oceans, are very important for ocean circulation and material exchange in the oceans. These rotating and propagating water masses[4] have a horizonal scale of about 100 km, a vertical scale of about 1000 m and a lifespan ranging from weeks to years. Mesoscale eddies are accompanied by temperature and salinity anomalies,[5,6] resulting in abnormal sound speed fields. Therefore, it is crucial to study of effects of mesoscale eddies on the sound field and spatial coherence.

In the past several decades, the influence of mesoscale eddies on the sound field has concerned both acousticians and oceanographers. The early studies that started in the 1970s were mainly based on the results of acoustic numerical modeling and theory derivation. Some classic features were discovered about the effects of eddies on transmission loss (TL),[7] the convergence zone,[8] refraction,[9] and time delay.[10] With the development of theoretical acoustic models and underwater acoustic experiments in deep water, many features have been interpreted theoretically and validated with *in situ* acoustic data and synchronous hydrographic data.[11,12] It has been found that mesoscale eddies can change the normal modes or the propagation path of acoustic rays. Meanwhile, the impacts of mesoscale eddies on long-range acoustic deflection, pulse width and arrival patterns have also been studied using high-resolution ocean reanalysis data or ocean models,[13,14] indicating that the eddies make the arrival patterns of sound fields complex so that it is hard to resolve individual arrivals.

However, little of this prior work has been about the effects of eddies on acoustic spatial coherence. In this paper, horizontal and vertical coherence in cold or warm eddy environments is studied, and variations of the horizontal correlation radius (HCR) and vertical correlation radius (VCR) with range and depth are also analyzed. In addition, the mechanism of propagation is analyzed from the phase and amplitude terms of the complex pressure.

This paper is organized as follows. Section 2 introduces the methods for construction of mesoscale eddy environments, calculation of correlation coefficients and the model configuration. The numerical results are presented in Section 3. In Section 4, discussion and interpretation of the results are provided. The main conclusions are presented in Section 5.

[†]Corresponding author. E-mail: gao-f21@mails.tsinghua.edu.cn

© 2022 Chinese Physical Society and IOP Publishing Ltd

2. Model and method

2.1. Construction of the eddy environment

Mesoscale eddies can be classified into cyclonic eddies and anticyclonic eddies. In the northern hemisphere, cyclonic eddies rotate anticlockwise with the temperature inside being often lower than that outside of the eddy range. The features of anticyclonic eddies are opposite to those of cyclonic eddies. Cyclonic (anticyclonic) eddies are also called cold (warm) eddies.

The three-dimensional structure of an eddy is often 'bullet-shaped',[15] with a radius at the subsurface bigger than that in deeper layers. In general, the temperature or salinity anomalies decay exponentially with distance from the eddy core. The maximum anomalies of temperature and salinity can be bigger than 7.7 °C and 1.0 psu (practical salinity unit), respectively, generating a sound speed anomaly of about 20.5 m/s.

The Gaussian eddy model is a simplified ideal hydrology model[16] that is widely used to describe the structure of mesoscale eddies and its effects on underwater acoustic propagation.[7,11,12] In a cylindrical coordinate system, the Gaussian eddy model comprises two simple parts

$$c(r,z) = c_0(z) + \Delta c(r,z), \tag{1}$$

where c_0 is the mean sound speed profile, which is a function of depth z and represents a range-independent environment for acoustic propagation. Δc is the sound speed perturbation term caused by the mesoscale eddy, and it is a function of z and range r. So, the results for c represent a range-dependent environment that contains sound speed perturbations superimposed on a deep-water sound speed profile. For the Munk sound speed profile, $c_0(z)$ can be expressed as

$$c_0(z) = 1500(1 + 0.0057(\mathrm{e}^{-\eta} - (1-\eta))), \tag{2}$$

$$\Delta c(r,z) = DC \times \exp\left[-\left(\frac{r-r_\mathrm{e}}{R}\right)^2 - \left(\frac{z-z_\mathrm{e}}{Z}\right)^2\right], \tag{3}$$

where $\eta = 2(z - z_{\mathrm{cx}})/z_{\mathrm{cx}}$, with z_{cx} being the depth of the deep-sea sound channel. DC is the intensity of the eddy, r_e and z_e are the locations of the eddy core and R and Z are, respectively, the horizontal and vertical radii of the eddy. According to the reported mesoscale eddy features,[4–6] eddy intensity DC, horizontal range r_e and vertical depth z_e of the eddy core, horizontal radius R and vertical radius Z are taken to be 10 m/s (warm eddy), −10 m/s (cold eddy), 50 km, 150 m, 50 km, and 700 m, respectively. The eddy environments calculated with a Gaussian eddy model are presented in Fig. 1.

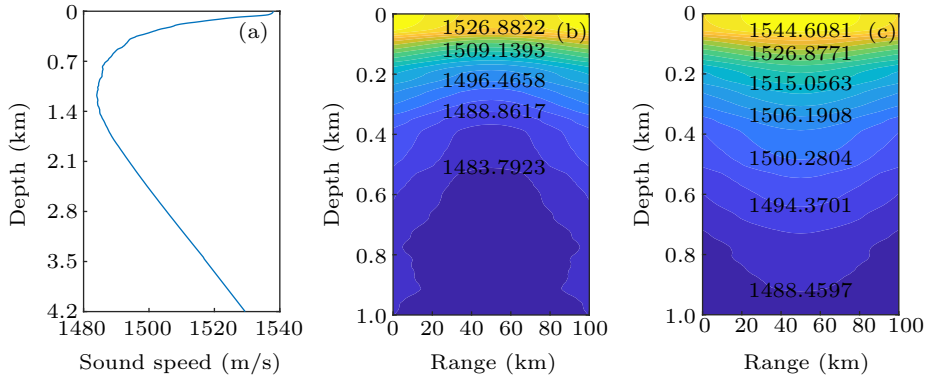


Fig. 1. Sound speed calculated based on a Gaussian eddy model: (a) observed mean sound speed profile, (b) cold eddy environment, (c) warm eddy environment.

The data shown in Fig. 1(a) represent a summer sound speed profile observed in the South China Sea. The sound speeds at the surface and bottom are 1538.2 m/s and 1529.4 m/s, and the minimum sound speed is 1484 m/s at a depth of 1180 m; it is an incomplete sound channel environment. The maximum sound speed perturbations in cold and warm eddy environments are 10 m/s and −10 m/s.

2.2. Model configuration and fundamental knowledge

Figure 2 shows a schematic of the numerical modeling configuration. The sound source is set at the edge of the eddy at a depth of 150 m and sound speed 1515.1 m/s, so the sound waves can propagate from outside to inside the eddy. With this configuration, the first convergence zone appears at about a range of 50 km from the source, close to the eddy core. Meanwhile, the horizontal sound speed gradient is monotonic, ranging from 0 km to 50 km. Therefore, the eddy has the maximum effect on the sound field.

The sea floor is set to be flat and the water depth is 4200 m. The parameters of the sediment layer are as follows: thickness 20 m, sound speed 1550 m/s, density 1.5 g/cm^3, attenuation coefficient 0.25 dB/λ. The parameters of the base layer are as follows: sound speed 1700 m/s, density 2.0 g/cm^3, attenuation coefficient 2 dB/λ.

It is necessary to provide some fundamental knowledge about the sound field structure and multipath patterns, which

are closely connected with the spatial coherence features analyzed in the following. The area for analysis is focused on a depth of 0 m–300 m and a range of 0 km–60 km. The complex sound field structure, in a no eddy environment, is shown in Fig. 3(a). It can be seen that the direct zone, the shadow zone and the convergence zone exist in the ranges 0 km–3 km, 3 km–48 km, and 48 km–60 km, respectively.

Since the amplitude of the reflected arrivals is much smaller than that of the direct arrivals, most energy in the direct and convergence zones is primarily from direct arrivals (Figs. 3(b) and 3(d)). The arrivals in the shadow zone are mainly made up of two groups of rays (Fig. 3(c)). Each ray group consists of bottom reflected rays and bottom–surface reflected rays. When both the source and receivers are in the shallower parts of deep water it is hard to distinguish the arrivals in each group.

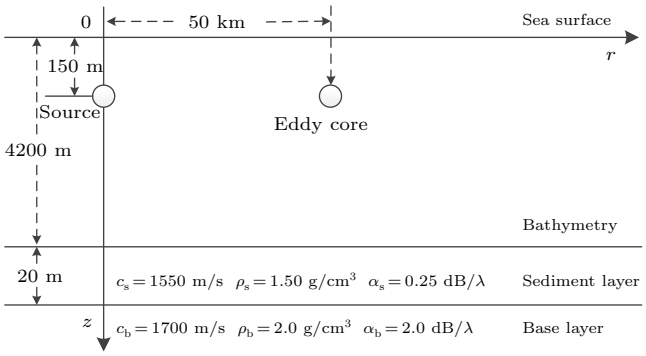


Fig. 2. A sketch map of acoustic numerical modeling in an eddy environment.

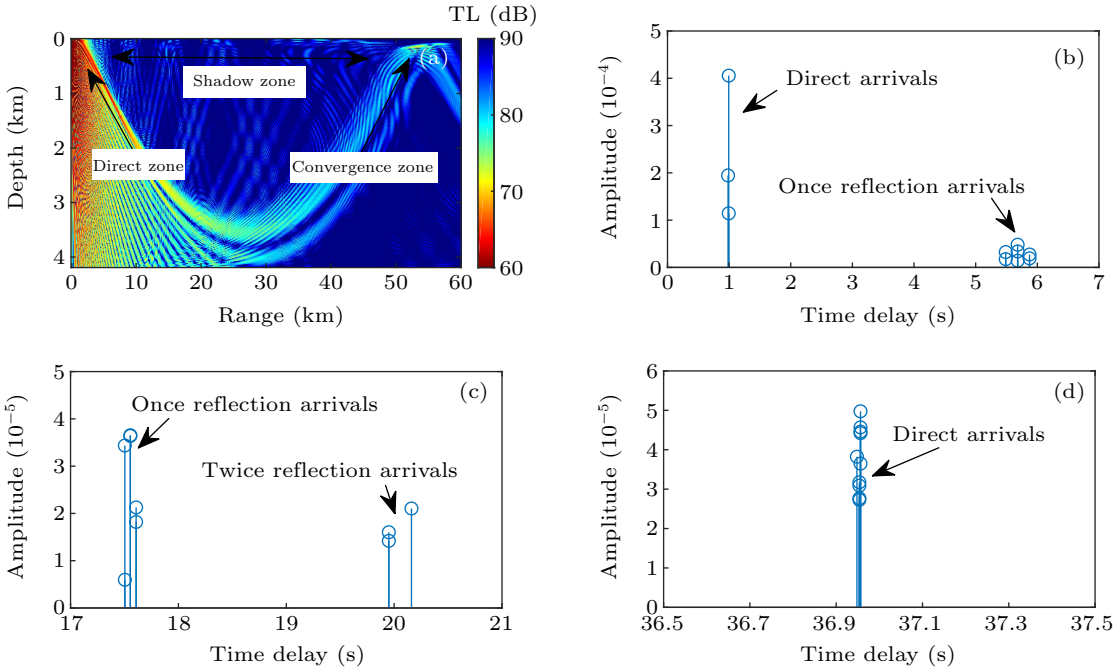


Fig. 3. Numerical results of TL versus range and depth (a) and amplitude versus time delay at a depth of 150 m at three different ranges: (b) 1.5 km, (c) 25 km, and (d) 55 km.

2.3. Coherence function

The coherence of underwater acoustic signals can be quantified by correlation coefficients and correlation radii. The correlation coefficient C of complex sound pressure p in the frequency domain is defined as[17]

$$C(r, r+\Delta r, z, z+\Delta z) = \max_{\phi_0} \frac{\mathrm{Re}\left(\int_{\omega_1}^{\omega_2} p_{r,z,\omega} p^*_{r+\Delta r,z+\Delta z,\omega} \mathrm{e}^{\mathrm{i}\phi_0} \mathrm{d}\omega\right)}{\sqrt{\int_{\omega_1}^{\omega_2} p_{r,z,\omega} p^*_{r,z,\omega} \mathrm{d}\omega \int_{\omega_1}^{\omega_2} p_{r+\Delta r,z+\Delta z,\omega} p^*_{r+\Delta r,z+\Delta z,\omega} \mathrm{d}\omega}}, \tag{4}$$

where $p_{r,z,\omega}$ and $p_{r+\Delta r,z+\Delta z,\omega}$ are the sound pressures of two different points (r, z) and $(r+\Delta r, z+\Delta z)$, r and z are the horizontal range and vertical depth in cylindrical coordinates, ω_1 and ω_2 are the lower and upper angular frequencies of the integral interval and * denotes complex conjugation. If $\Delta z = 0$, C represents the horizontal correlation coefficient. If $\Delta r = 0$, C represents the vertical correlation coefficient. The range or the depth are defined as the correlation radius, where C drops to less than 0.7. Re denotes the real part. $\mathrm{e}^{\mathrm{i}\phi_0}$ is the phase correction term to obtain the maximum value of C, which is crucial for numerical calculation.

The parabolic equation (PE) theory model and ray theory model are used in this work. The PE model can handle sound speed with horizontal variation and achieve high precision with calculation stability, fit for modeling acoustic propagation in the range-dependent environment of a mesoscale eddy. The ray model calculates the time delay of different ar-

rivals with different source/receiver angles, providing data for feature analysis and interpretation.

We set the source frequency to be 175 Hz–225 Hz and the frequency interval to be 1 Hz, and ran the acoustic model with different source frequencies in cold eddy, no eddy and warm eddy environments to obtain the sound pressure.

3. Numerical results

This section presents the numerical results for horizontal and vertical coherence. Due to the close connection of the high-intensity zone with spatial coherence, the effects of a mesoscale eddy on spatial coherence in the shadow zone and high-intensity zone are analyzed separately.

3.1. Horizontal coherence

Figure 4 shows the horizontal correlation coefficients in cold, no and warm eddy environments in the range of 0 km–45 km. In all subplots, the correlation coefficient contours vary from 0.7 (equal to the coherence radius) to 1, with a horizontal range of 0 km–45 km from the source and a horizontal separation of 0 m–600 m.

It can be seen that the horizontal coefficient oscillates with range and horizontal separation, consistent with the findings of previous studies.[18,19] The sound field in the direct zone is strongly correlated and the HCR is greater than 1 km. The direct zone appears at the edge of the eddy, so the effect of eddies on the HCR in the direct zone is very weak.

Comparing the subplots in Fig. 4, it can be seen that the horizontal coefficient increases significantly with range and decreases rapidly with depth. At a depth of 150 m in the no eddy environment (Fig. 4(e)), the HCR increases from 0 m to 634 m over a horizontal range of 3 km–36 km. At the same time, the HCR in the 25 km range in the no eddy environment drops from 381 m (Fig. 4(b)) to 141 m (Fig. 4(h)). It should be noted that the numerical modeling is carried out in the absence of noise, and spatial coherence in the far field will decrease due to the smaller SNR in real ocean environments.

Comparing the horizontal coefficients in Fig. 4 in different environments, it is found that the differences are not so significant in the near field and become apparent as the range increases. According to the model configuration in Subsection 2.2, the source is 50 km from the eddy core and the sound pressure disturbance increases with propagation toward the eddy core, resulting in larger differences in the coherence coefficients in different eddy environments.

To verify this conclusion, another simulation experiment was carried out using the same environment as before, while the source was placed at the eddy core and the sound allowed propagate outward from the eddy core; the numerical results are shown in Fig. 5. When the source is at the eddy core, the differences in the horizontal coefficient between different eddy environments are larger compared with when the source is placed at the edge of the eddy.

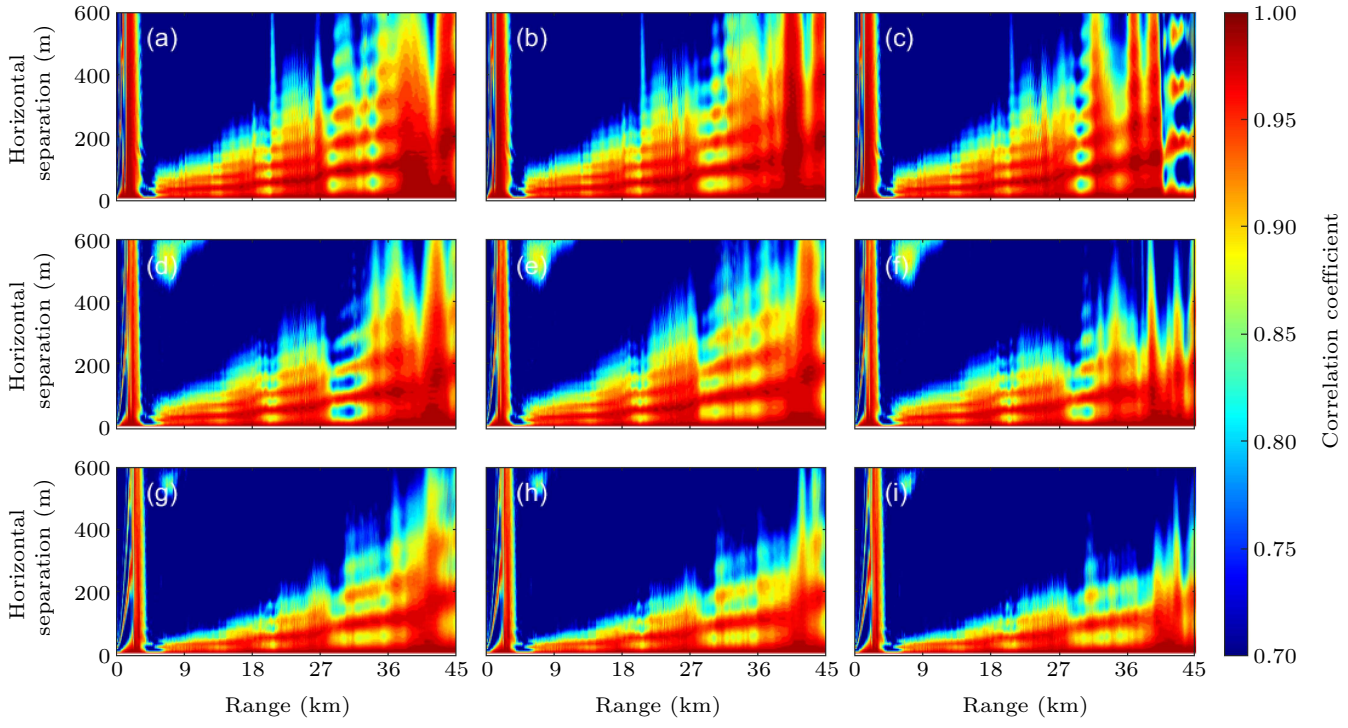


Fig. 4. Horizontal correlation coefficients in the shadow zone in cold, no and warm eddy environments (panels from left to right) at three receiver depths: (a)–(c) 50 m, (d)–(f) 150 m, and (g)–(i) 300 m.

In addition, the HCR in the warm eddy environment is the greatest when the source is at the edge of the eddy, while it is smallest when the source is at the eddy core, due to the opposite sound speed gradient.

Figure 6 shows the horizontal correlation coefficients near and in the convergence zone (range 45 km–60 km) for different environments. The HCR becomes complex with depth, range and environment, and is closely related to the spatial variability of the convergence zone. First, the horizontal coherence is strong and the maximum HCR can be larger than 2 km, consistent with the findings in Ref. [20]. Second, cold eddies can bring a larger HCR to shallower depths (Fig. 6(a)), and the larger HCR range increases sequentially in cold, no and warm eddy environments (Figs. 6(d)–6(f)). Third, two HCR peaks appear at ranges of 49 km and 58 km for the no eddy environment with a horizontal shadow between them (Fig. 6(g)), and in the no and warm eddy environments their positions move toward a larger range (Figs. 6(h) and 6(i)).

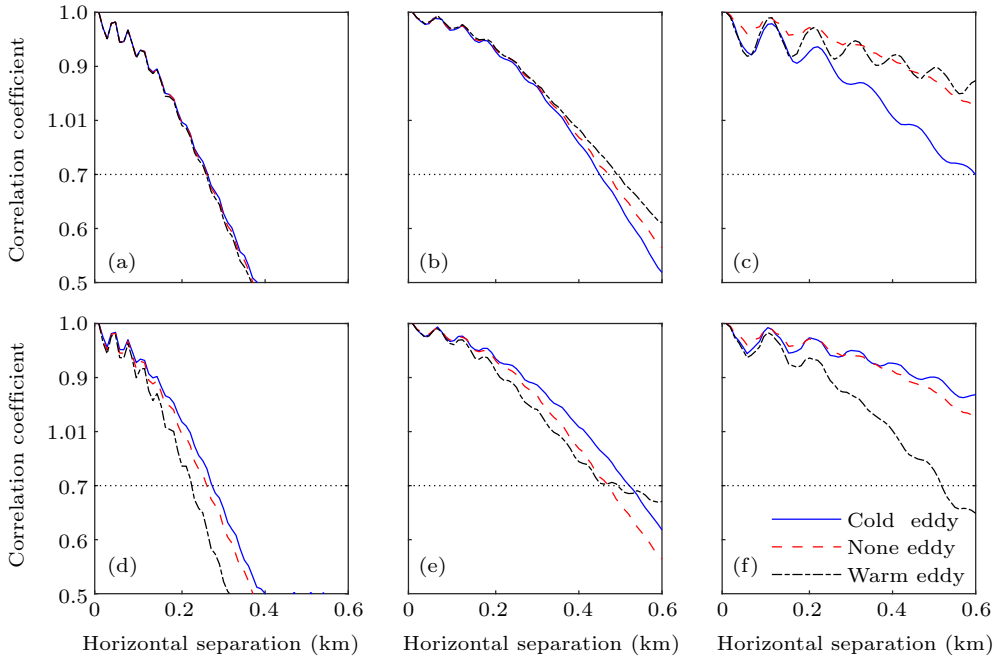


Fig. 5. Correlation coefficients versus horizontal separation for two source–receiver configurations at three receiver ranges: (a)–(c) are at receiver ranges of 15 km, 20 km, and 35 km, respectively, with the source at the eddy edge; and (d)–(f) are at receiver ranges of 15 km, 20 km, and 35 km, respectively, with the source at the eddy core.

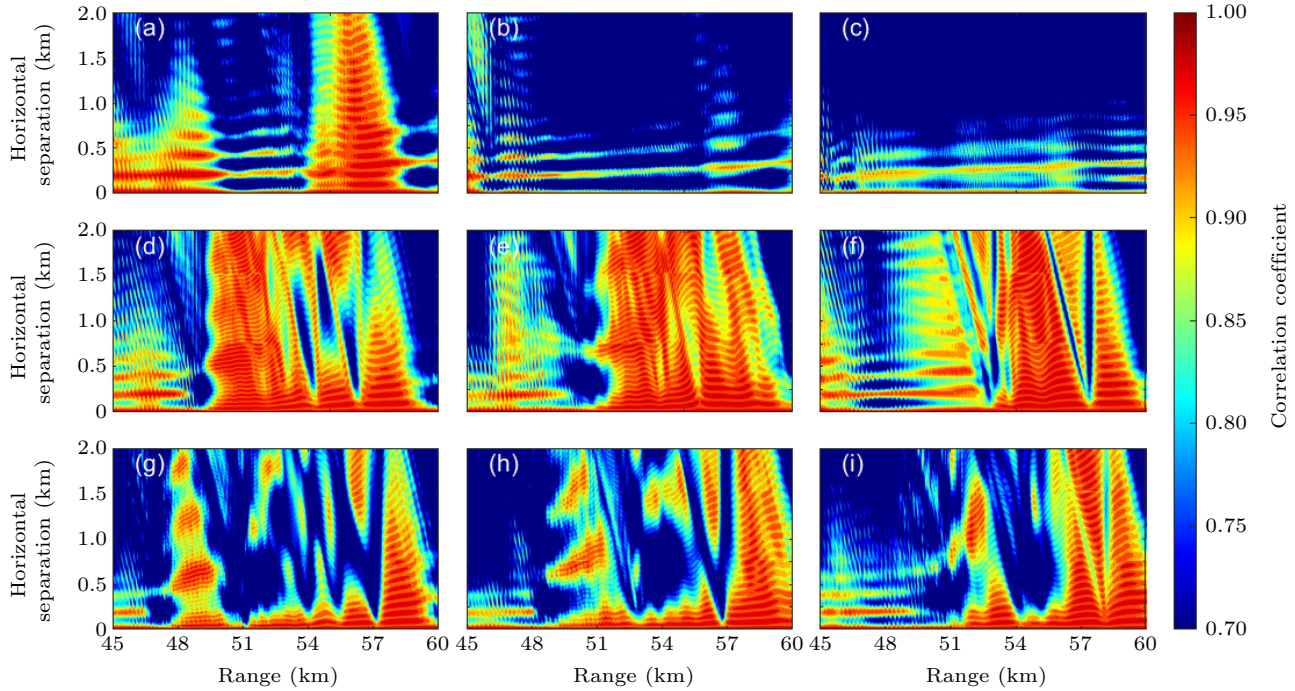


Fig. 6. Horizontal correlation coefficients in the convergence zone in cold, no and warm eddy environments (panels from left to right) at three receiver depths: (a)–(c) 50 m, (d)–(f) 150 m, and (g)–(i) 300 m.

3.2. Vertical coherence

Figure 7 shows the vertical correlation coefficients in the shadow zone at three ranges, 15 km, 25 km, and 35 km, in cold, no and warm eddy environments, respectively. By comparing the subplots of different ranges in Fig. 7 it can be seen that the VCR also increases with range and decreases with depth, and differences in VCR between different eddy environments increase with range. The VCR in the warm eddy environment is the biggest, corresponding to the variation features of HCR analyzed above.

Figure 8 shows the vertical correlation coefficients in the convergence zone at two reference ranges, 53 km and 58 km, in cold, no and warm eddy environments, respectively. Overall, the vertical coherence is much stronger than in the shadow zone, and the correlation coefficients increase with depth. By comparing the VCR in different eddy environments, it can be seen that cold eddies make the VCR shallower and warm eddies deepen it. For example, the strong vertical coherence layer starts from depths of 38 m, 60 m, and 80 m in cold, no and warm eddy environments, respectively.

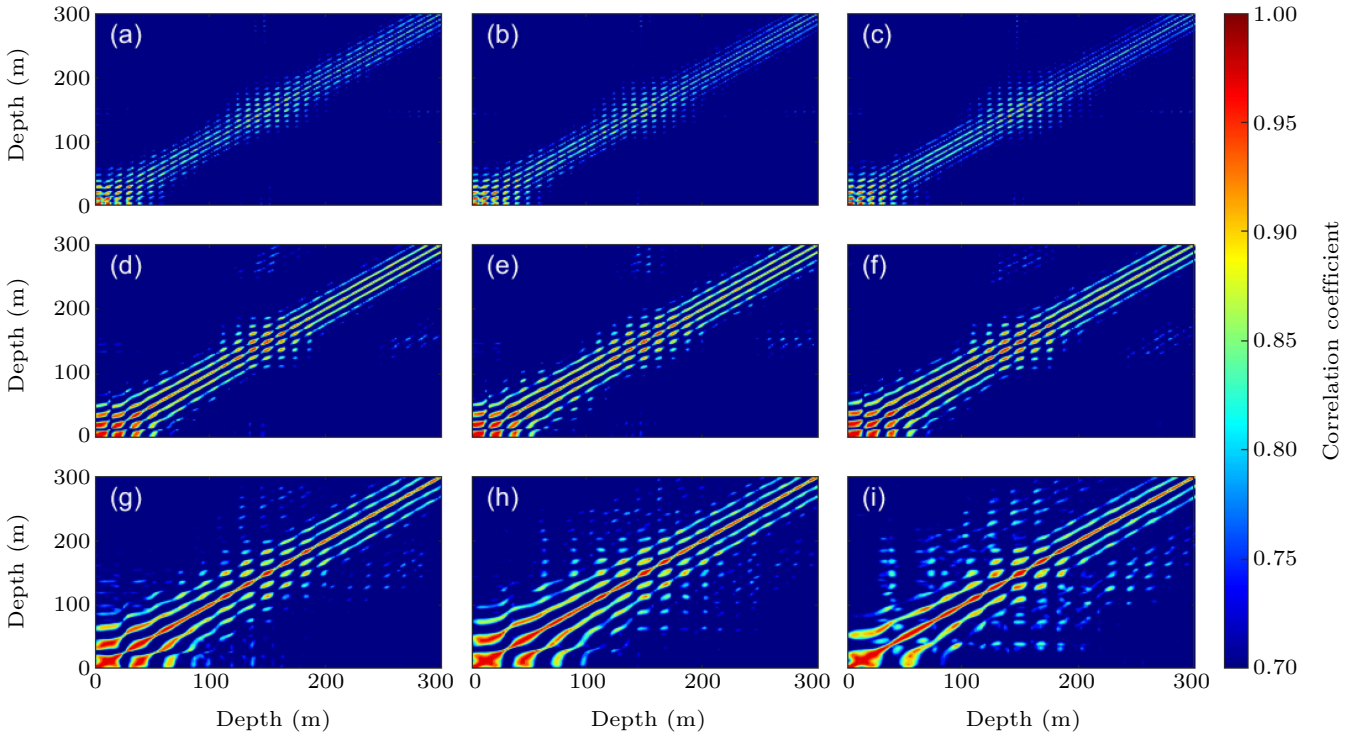


Fig. 7. Vertical correlation coefficients (shaded) in the shadow zone in cold, no and warm eddy environments (panels from left to right) at three receiver ranges: (a)–(c) 15 km, (d)–(f) 25 km, and (g)–(i) 35 km.

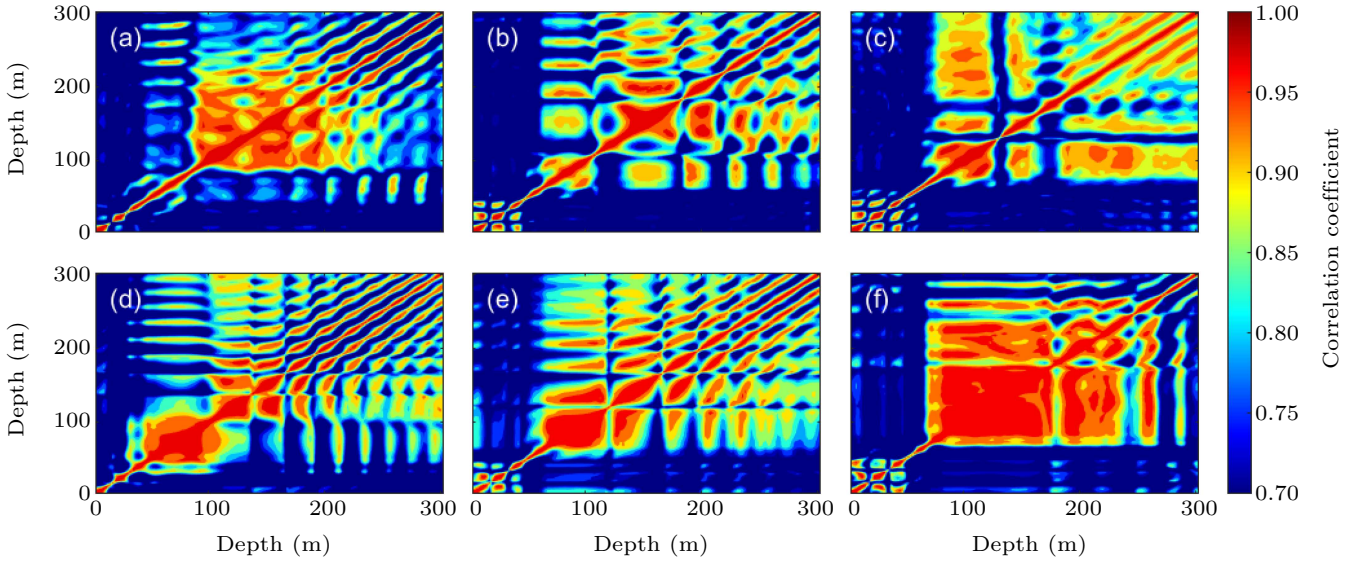


Fig. 8. Vertical correlation coefficients (shaded) in the convergence zone in cold, no and warm eddy environments (panels from left to right) at two receiver ranges: (a)–(c) 53 km and (d)–(f) 58 km.

4. Discussion

The complex pressure p at the site (r, z) and angular frequency ω can be written in the form of a product of a slowly evolving amplitude A and a rapid changing phase ϕ

$$p_{r,\omega} = A_{r,\omega} \mathrm{e}^{\mathrm{i}\phi_{r,\omega}}, \tag{5}$$

where the subscript z is omitted for simplicity. By substituting Eq. (5) into Eq. (4), the correlation coefficient takes the form

$$C(r, r+\Delta r) = \max_{\phi_0} \frac{\mathrm{Re}\left(\sum_{n=1}^{N} A_{r,\omega_n} \mathrm{e}^{\mathrm{i}\phi_{r,\omega_n}} A_{r+\Delta r,\omega_n} \mathrm{e}^{-\mathrm{i}\phi_{r+\Delta r,\omega_n}} \mathrm{e}^{\mathrm{i}\phi_0}\right)}{\sqrt{\left(\sum_{n=1}^{N} A_{r,\omega_n}^2\right)\left(\sum_{n=1}^{N} A_{r+\Delta r,\omega_n}^2\right)}}, \tag{6}$$

where $n = 1, 2, \ldots, N$, N being the total number of ω points to be calculated. Set the mth arrival $p_{r,\omega,m} = A_{r,\omega,m} \mathrm{e}^{\mathrm{i}\phi_{r,\omega,m}}$ and p is the sum of multipath arrivals

$$p_{r,\omega} = \sum_{m=1}^{M} A_{r,\omega,m} \mathrm{e}^{\mathrm{i}\phi_{r,\omega,m}}, \tag{7}$$

where $m = 1, 2, \ldots, M$, M being the total number of arrivals, and it can be seen that the amplitude and phase of $p_{r,\omega}$ are affected by each arrival. Substituting the multipath complex pressure from Eq. (7) into Eq. (6), the correlation coefficient is calculated as

$$C(r, r+\Delta r) = \max_{\phi_0} \frac{\mathrm{Re}\left[\sum_{n=1}^{N}\left(\left(\sum_{m=1}^{M} A_{r,\omega_n,m} \mathrm{e}^{\mathrm{i}\phi_{r,\omega_n,m}}\right)\left(\sum_{m=1}^{M} A_{r+\Delta r,\omega_n,m} \mathrm{e}^{-\mathrm{i}\phi_{r+\Delta r,\omega_n,m}}\right)\mathrm{e}^{\mathrm{i}\phi_0}\right)\right]}{\sqrt{\left(\sum_{n=1}^{N}\sum_{m=1}^{M} A_{r,\omega_n,m}^2\right)\left(\sum_{n=1}^{N}\sum_{m=1}^{M} A_{r+\Delta r,\omega_n,m}^2\right)}}. \tag{8}$$

The multipath arrivals are divided into two groups of eigenrays, group 1 containing only arrivals that do not interact with the boundary and group 2 containing arrivals that are reflected from the surface or the bottom boundary.

Under realistic conditions, the multipath arrivals received by a hydrophone can be divided into two main cases: the first case is that multipath arrivals, including group 1 and group 2, are received, which is the actual situation in the high intensity zone; the second case is when only the eigenrays of group 2 are received, and this is consistent with the shadow zone.

4.1. Interpretation for the high intensity zone

Considering the first case, a hydrophone receives multipath arrivals, including group 1 and group 2, with group 1 having a much larger amplitude than group 2 ($A_{r,\omega,\text{group 1}} \gg A_{r,\omega,\text{group 2}}$), i.e., $A_{r,\omega} \approx A_{r,\omega,\text{group 1}}$, $\phi_{r,\omega} \approx \phi_{r,\omega,\text{group 1}}$, and $\phi_{r+\Delta r,\omega} \approx \phi_{r+\Delta r,\omega,\text{group 1}}$, and this corresponds to the real conditions in the high-intensity zone.

If the volume attenuation of water absorption is neglected, the amplitude term $A_{r,\omega,\text{group 1}}$ evolves slowly in small range of narrow angular frequency bands (Fig. 9(a)), so $A_{r,\omega,\text{group 1}} \approx A_{r+\Delta r,\omega+\Delta\omega,\text{group 1}}$. Then, $p_{r,\omega} \approx A_{r,\omega,\text{group 1}} \mathrm{e}^{\mathrm{i}\phi_{r,\omega,\text{group 1}}}$ and $p_{r+\Delta r,\omega+\Delta\omega} \approx A_{r,\omega,\text{group 1}} \mathrm{e}^{\mathrm{i}\phi_{r+\Delta r,\omega+\Delta\omega,\text{group 1}}}$. One can simplify Eq. (8) as

$$C_{r,r+\Delta r} = \max_{\phi_0} \frac{1}{N} \sum_{\omega_1}^{\omega_2} \cos\phi, \tag{9}$$

where $\phi = \phi_{r,\omega} - \phi_{r+\Delta r,\omega} + \phi_0$. Then, the correlation coefficient function is only related to the function $\cos(\cdot)$. The phase $\phi_{r,\omega}$ and $\phi_{r+\Delta r,\omega}$, for group 1, is just the function of angular frequency and arrival time, which varies periodically and decreases uniformly with increasing angular frequency (Fig. 9(b)). Since the eigenray propagates without interaction with the boundary, $\phi_{r,\omega}$ depends only on the arriving time delay τ_r. Setting $\phi_{r,\omega} = (\omega_1 + (n-1)\Delta\omega)\tau_r$ and $\phi_{r+\Delta r,\omega} = (\omega_1 + (n-1)\Delta\omega)\tau_{r+\Delta r}$, equation (9) can be given by

$$C_{r,r+\Delta r} = \max_{\phi_0} \frac{1}{N} \sum_{n=1}^{N} \cos\left[(\omega_1 + (n-1)\Delta\omega)\Delta\tau_{r,r+\Delta r} - \phi_0\right], \tag{10}$$

where $\Delta\tau_{r,r+\Delta r}$ is the relative time delay between two different receivers and $\Delta\omega$ is the angular frequency interval. If the angular frequency band and interval are fixed, the spatial coherence will depend on $\Delta\tau_{r,,r+\Delta r}$. By adjusting ϕ_0, the maximum $C_{r,r+\Delta r}$ can be obtained. Equation (10) is suitable for explaining the strong spatial coherence in the direct and convergence zones (Fig. 9(c)), which can also be interpreted as a high-intensity zone leading to high spatial coherence.

Many papers on the effect of mesoscale eddies on acoustic propagation have reported that the location (range and depth) and width of the convergence zone change in a mesoscale eddy environment. The simulation results of TL, with a source frequency of 200 Hz according to the environments in Fig. 1 and model configuration in Fig. 2, are presented in Fig. 10, in which the blue and white lines are the direct rays and bottom reflected rays, respectively.

Mesoscale eddies lead to fluctuations of the sound speed in the horizontal direction, which changes the reversal depth

of the ray. In a cold eddy environment, the sound speed gradually decreases in the horizontal direction from the source to the eddy core, making the reversal depth shallower. Apparently, a cold eddy brings the convergence zone closer to the source by about 2.2 km, moving it up towards the sea surface by about 30 m, and reduces its width (Fig. 10(a)) compared with the no eddy environment (Fig. 10(b)). The influence of a warm eddy environment on the convergence zone is opposite to that of a cold eddy (Fig. 10(c)). Based on the close connection between the convergence zone and high spatial coherence, the influence of mesoscale eddies on the spatial coherence of the high-intensity zone can be well explained.

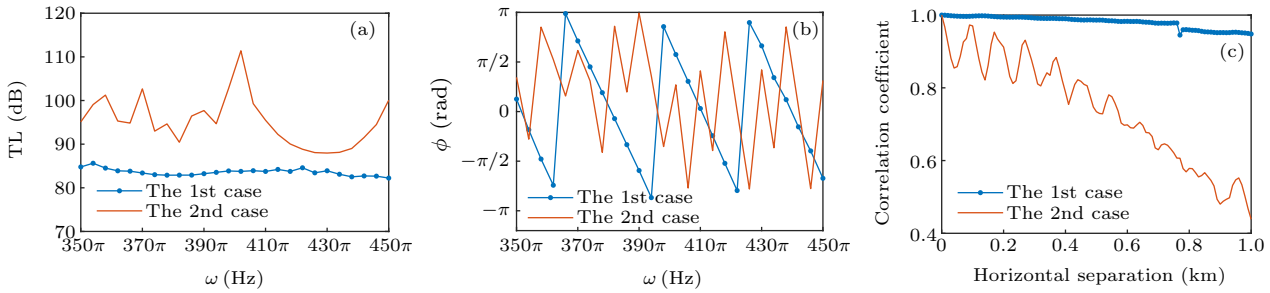


Fig. 9. Comparison of the results of the two cases: (a) TL versus angular frequency, (b) phase versus angular frequency, (c) correlation coefficient versus horizontal separation.

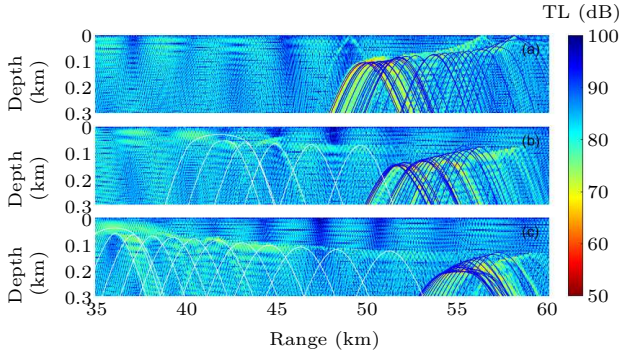


Fig. 10. TL versus range and depth in different environments: (a) cold eddy environment, (b) no eddy environment, and (c) warm eddy environment.

4.2. Interpretation for shadow zone

Considering the second case, only group 2 eigenrays are received by the receiver, and it this corresponds to real conditions in the shadow zone. $p_{r,\omega}$ in Eq. (7) depends on more arrivals along a different path. $A_{r,\omega}$ and $\phi_{r,\omega}$ become complicated and disordered over an angular frequency band (Figs. 9(a) and 9(b)) as a consequence of boundary reflection, volume refraction and absorption, etc., resulting in a rapid decay of spatial coherence (Fig. 9(c)).

The $A_{r,\omega,m}$ and $\phi_{r,\omega,m}$ in the shadow zone vary with horizontal range, angular frequency and propagation path. The simplified method for deriving Eq. (8) in Subsection 4.1 is not appropriate for the shadow zone, so it is hard to obtain a simple form to quantify the characteristics of the spatial coherence.

A simple numerical experiment is carried out to compare the influence of $A_{r,\omega}$ and $\phi_{r,\omega}$ on the correlation coefficient by calculating C, C_ϕ with $A_{r,\omega} = 1$ and C_A with $\phi_{r,\omega} = 0$. Figure 11 shows the correlation coefficients versus horizontal separation for depth 150 m at three receiver ranges, 10 km, 25 km, and 45 km, in a no eddy environment with a source frequency of 200 Hz.

Three apparent features can be concluded by comparing C, C_ϕ, and C_A. Firstly, the curves for C_ϕ increase with range and are similar to C as a whole, which corresponds to the features of horizontal coherence in Fig. 4(a). Secondly, the curves for C_A are larger than for C, and C_A decreases with range. Thirdly, C_ϕ varies much faster than C_A, especially for the near field. Overall, $\phi_{r,\omega}$ is the main factor affecting C, compared with $A_{r,\omega}$.

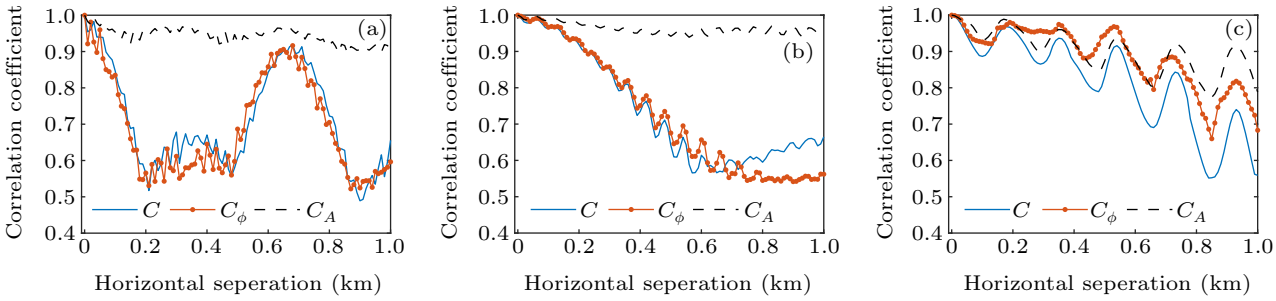


Fig. 11. Correlation coefficient versus horizontal separation of at three receiver ranges: (a) 10 km, (b) 25 km, and (c) 45 km.

Based on the conclusions above, a possible explanation for the physical mechanism of the variation of spatial coherence with range and depth is provided, which is focused on $\phi_{r,\omega}$ and multipath structures.

In general, most of the energy of the complex pressure $p_{r,\omega}$, in the shadow zone comes from two sets of ar-

rivals, the once-reflected arrivals and the twice-reflected arrivals (Fig. 3(c)). If the eigenrays are reflected from the boundary more than twice, their complex sound pressure is far less than the first two sets of arrivals and their effects on $\phi_{r,\omega}$ can be neglected. Since the variation of the relative time delay $\Delta\tau$ between the arrivals is similar, the $\Delta\tau$ of the first set of arrivals, which consist of bottom reflected arrivals and bottom-surface reflected arrivals, is taken for the analysis. $\Delta\tau$ is calculated using the ray theory model with a source frequency of 200 Hz.

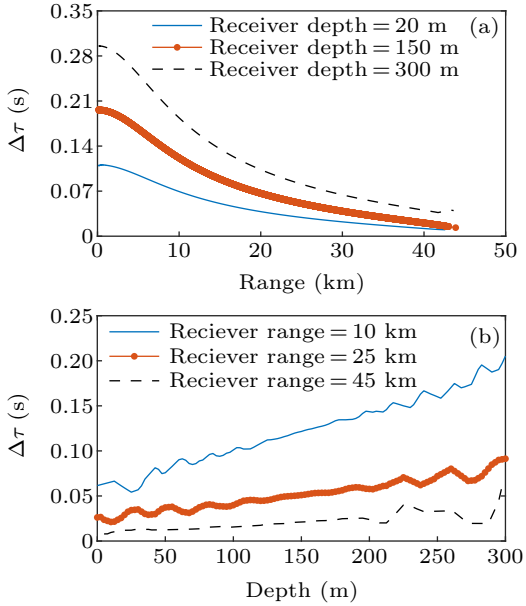


Fig. 12. Relative time delay ($\Delta\tau$) of multipath arrivals: (a) $\Delta\tau$ versus range and (b) $\Delta\tau$ versus depth.

Figure 12(a) shows the relative time delay ($\Delta\tau_{r,\omega} = \tau_{r,\omega,2} - \tau_{r,\omega,1}$) versus range at three receiver depths, 20 m, 150 m, and 300 m, and it can be seen that $\Delta\tau$ decreases with range, i.e., the shallower the receiver depth, the smaller $\Delta\tau$. Figure 12(b) shows the relative time delay ($\Delta\tau_{z,\omega} = \tau_{z,\omega,2} - \tau_{z,\omega,1}$) versus depth for three receiver ranges, 10 km, 25 km, and 45 km, and it is seen that $\Delta\tau$ increases with depth, i.e. the further the receiver range, the smaller $\Delta\tau$. A smaller $\Delta\tau$ indicates a shorter length of time for which the acoustic pulse is in the time domain, which implies simpler multipath structures and a slower spatial variation of $\phi_{r,\omega}$, leading to higher spatial coherence.

In addition, the number of arrivals decreases with range, because the eigenrays of large source angles decay rapidly and cannot propagate to the far field; this also leads to simpler multipath structures and higher spatial coherence.

The coherent TL reflects multipath interference, and the more complex multipath structure leads to smaller spatial intervals of TL stripes and correlation lengths. To show more clearly the TL stripe of the shadow zone, figure 13 presents the 200 Hz sound field for a 50 m thick surface layer. It can be found that the spatial intervals of TL stripes decrease with increasing depth and increase with increasing range, which is consistent with the variation features of HCR and VCR analyzed above.

In addition, the spatial intervals of TL stripes are the largest in a warm eddy environment compared with cold eddy and no eddy environments, which can well explain the characteristics of HCR and VCR influenced by mesoscale eddies.

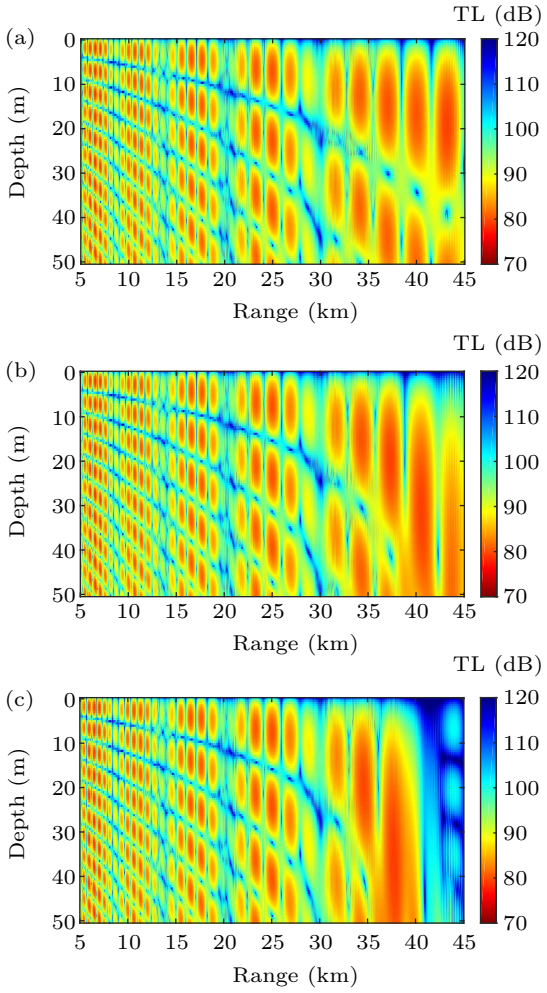


Fig. 13. Coherent TL versus range and depth in the shadow zone in cold (a), no (b) and warm (c) eddy environments.

5. Conclusion

This paper presents insights into spatial coherence and its physical mechanism in medium ranges through mesoscale eddy environments. The results are given by numerical simulation using an empirical formula for mesoscale eddy environments and an acoustic numerical model for sound fields. The experimental configuration is designed to make acoustic waves propagate from outside to inside the mesoscale eddy, and allows the first convergence zone to be close to the eddy core. Several key conclusions are obtained as follows.

First, the spatial coherence is closely connected with multipath structures; a simpler multipath structure results in regular phase variation and unchanging amplitude over the angular frequency integral interval. The phase of the complex pressure is the main factor affecting spatial coherence compared

with the amplitude. In addition, the phase depends on the main arrivals of the multipath structure.

Second, a mesoscale eddy changes the location and width of the convergence zone, thus significantly affecting spatial coherence in the high-intensity zone. The influences on spatial coherence from cold and warm eddies are opposite, and warm eddies deepen and widen the strongly correlated area, which also improves spatial coherence.

Third, a warm eddy environment increases the HCR and VCR while a cold eddy decreases them. HCR and VCR increase with range and decrease with depth, which can be interpreted by the spatial intervals of TL stripes and relative time delay between the bottom reflection arrival and bottom surface reflection arrival.

It should be noted that the results and conclusions are obtained based on the numerical configuration. The source/receiver/mesoscale eddy geometry and the intensity, radius and depth of the mesoscale eddy are all important parameters affecting the spatial coherence. Therefore, we have paid attention to the general features and their physical mechanism and do not provide quantified results.

Acknowledgments

Project supported by the National Key Research and Development Program of China (Grant No. 2020YFA0607900), the National Natural Science Foundation of China (Grant Nos. 42176019 and 11874061), and the Youth Innovation Promotion Association CAS (Grant No. 2021023).

The authors are grateful to Chinese Academy of Sciences, Institute of Acoustics and personally to Dr Mengyuan Wang and Fanchen Dong for the provision of correlation coefficient code and discussions. The authors also wish to thank Dr Jun Li of the China State Shipbuilding Corporation and Dr Peng Xiao of the Southern Marine Science and Engineering Guangdong Laboratory for useful advice about the manuscript.

References

[1] Li Z L, Dong F C, Hu Z G and Wu S L 2019 *Acta Phys. Sin.* **68** 134305 (in Chinese)
[2] Duda T F, Collis J M, Lin Y T, Newhall A E, Lynch J F and Harry A D 2012 *J. Acoust. Soc. Am.* **131** 1782
[3] Zhou S, Zhang R, Tao X, Gong M and Hao L 1998 *Progress in Natural Science* **8** 292
[4] Chelton D B, Schlax M G and Samelson R M 2011 *Progr. Oceanogr.* **91** 167
[5] Zhang Y, Chen X and Dong C 2019 *Atmosphere* **10** 553
[6] Keppler L, Cravatte S, Chaigneau A, Pegliasco C, Gourdeau L and Singh A 2018 *J. Geophys. Res. Oceans* **123** 2731
[7] Jian Y J, Zhang J, Liu Q S and Wang Y F 2009 *Appl. Acoust.* **70** 432
[8] Lawrence M W 1983 *J. Acoust. Soc. Am.* **73** 474
[9] Weinberg N L and Clark J G 1980 *J. Acoust. Soc. Am.* **68** 703
[10] Mellberg L E, Robinson A R and Botseas G 1990 *J. Acoust. Soc. Am.* **87** 1044
[11] Xiao Y, Li Z L, Li J, Liu J Q and Sabra K G 2019 *Chin. Phys. B* **28** 054301
[12] Liu J, Piao S, Gong L, Zhang M, Guo Y and Zhang S 2021 *J. Mar. Sci. Eng.* **9** 787
[13] Heaney K D and Campbell R L 2016 *J. Acoust. Soc. Am.* **139** 918
[14] Geyer F, Sagen H, Cornuelle B, Mazloff M R and Vazquez H J 2020 *J. Acoust. Soc. Am.* **147** 1042
[15] Sun W, Dong C, Wang R, Liu Y and Yu K 2017 *J. Geophys. Res. Oceans* **122** 1476
[16] Calado L, A Gangopadhyay and da Silveira I C A 2006 *Geophys. Res. Lett.* **33** L12602
[17] Wang Q and Zhang R H 1992 *J. Acoust. Soc. Am.* **92** 932
[18] Yang K D, Li H and Duan R 2017 *Chin. Phys. Lett.* **34** 024301
[19] Li H, Yang K D, Lei Z X and Duan R 2017 *Acoust. Aust.* **45** 529
[20] Li J, Li Z L and Ren Y 2016 *Chin. Phys. B* **25** 124310